Boundary-Layer Meteorol (2014) 151:293–315
DOI 10.1007/s10546-013-9894-y

ARTICLE

On the Influence of a Simple Microphysics Parametrization on Radiation Fog Modelling: A Case Study During ParisFog

Xiaojing Zhang · Luc Musson-Genon · Eric Dupont · Maya Milliez · Bertrand Carissimo

Received: 24 October 2012 / Accepted: 7 December 2013 / Published online: 4 January 2014

Abstract A detailed numerical simulation of a radiation fog event with a single column model is presented, which takes into account recent developments in microphysical parametrizations. One-dimensional simulations are performed using the computational fluid dynamics model *Code_Saturne* and the results are compared to a very detailed in situ dataset collected during the ParisFog campaign, which took place near Paris, France, during the winter 2006–2007. Special attention is given to the detailed and complete diurnal simulations and to the role of microphysics in the fog life cycle. The comparison between the simulated and the observed visibility, in the single-column model case study, shows that the evolution of radiation fog is correctly simulated. Sensitivity simulations show that fog development and dissipation are sensitive to the droplet-size distribution through sedimentation/deposition processes but the aerosol number concentration in the coarse mode has a low impact on the time of fog formation.

Keywords Droplet deposition · Fog modelling · Nucleation · Radiation fog · Sedimentation · Semi-spectral microphysics

1 Introduction

Fog is an important meteorological phenomenon, which can have significant impacts on air quality, airport operations, and highway safety, and therefore have economic impacts (Gultepe et al. 2009). Radiative cooling is one of the major processes leading to fog formation and development over continental areas. Radiation fog formation is primarily controlled by the cooling of moist air by longwave radiation and the vertical mixing of heat and moisture including interaction with the land surface. Its development may be further influenced by longwave cooling and turbulence entrainment–detrainment at the top of the fog layer, and by microphysical processes through droplet activation. Its dissipation is then driven by the

---

X. Zhang · L. Musson-Genon (✉) · E. Dupont · M. Milliez · B. Carissimo
CEREA: Atmospheric Environment Teaching and Research Center, Joint Laboratory École des Ponts ParisTech-EDF R&D, Université Paris-Est, EDF R&D, 6 Quai Watier, BP 49, 78401 Chatou Cedex, France
e-mail: luc.musson-genon@edf.fr

gravitational settling of fog droplets, longwave radiative cooling and shortwave warming of the air close to the surface.

In recent years, there has been important progress in fog simulation and prediction using single-column models that provide sufficiently fine vertical resolution to describe these complex mechanisms (Tardif 2007). In ensemble forecast and assimilation systems, single-column models are used to provide accurate forecasting of fog events (Bott and Trautmann 2002; Bergot et al. 2005; Müller et al. 2007; Roquelaure and Bergot 2008). A comparison of such models shows significant variability in the predicted times of fog formation and dissipation (Bergot et al. 2007). Some experimental data have been used for model validation such as data from campaigns in Albany, New York, USA during the Fog82 experiment (Meyer et al. 1986), Cabauw in the Netherlands (Musson-Genon 1987; Duynkerke 1991; Nakanishi 2000), Lille in northern France (Guedalia and Bergot 1994), the Po Valley in northern Italy (Fuzzi et al. 1992, 1998) and Cardington, UK (Price 2011). Recently, a 6-month cooperative field experiment, named ParisFog, was conducted at the SIRTA Observatory (Site Instrumental de Recherche en Télédétection Atmosphérique, French acronym for instrumented site for atmospheric remote sensing research) located 20 km south of Paris, France, from November 2006 to March 2007 devoted to the simultaneous monitoring of all important processes in the fog life cycle (Haeffelin et al. 2010).

The aim of this paper is to contribute to improving the modelling of radiation fog. For that it is important to identify the physical processes that play a key role in its formation, vertical extension and dissipation. For instance, recently, Porson et al. (2011) studied the key features that control fog modelling, focusing their study on the change in static stability; Bott (1991) showed by a model sensitivity analysis that the fog life cycle, from formation to dissipation, is very sensitive to the different types of aerosol size distribution (e.g., urban, rural, marine); and Rangognio et al. (2009) showed that the aerosol particle number concentration is a key parameter for the accurate prediction of the microphysical properties of fog droplets and that it influences fog development, as observed during a well-documented case of Parisfog experimental field study. However, they did not study the dissipation phase.

As a complement to these studies, the present work focuses on the effects of fog-droplet size distribution on the entire fog life cycle from formation to dissipation. For that matter, sensitivity tests are performed with a single-column model that includes turbulence and radiation schemes, and a semi-spectral cloud scheme. We pay particular attention to the interactions between nucleation, sedimentation and deposition.

Indeed, the important role of fog-droplet sedimentation in the water budget of radiation fog was first revealed in field measurements as well as in numerical studies of Roach et al. (1976) and Brown and Roach (1976). Numerous parametrizations of droplet settling for fog and low-cloud modelling are available in the literature. They depend either on liquid water content (Brown and Roach 1976; Corradini and Tonna 1980; Kunkel 1984; Musson-Genon 1987; Duynkerke and Driedonks 1987) or on droplet radius and the application of Stokes law (Duynkerke 1991). This latest formulation is used because it is consistent with the description of a droplet-size distribution in fog modelling, and a slip correction factor for small fog droplets has been added in the Stokes law formulation following Pruppacher and Klett (1997).

Regarding deposition, the interactions with the ground surface should be an important factor as shown by Glasow and Bott (1999) for tall vegetation and by Klemm and Wrzesinsky (2007) for the water balance in ecosystems. These interactions increase the loss of fog droplets near the ground; they are modelled in the same manner as that for aerosol particles, following Zhang et al. (2001).

Fig. 1 Satellite view of the experimental SIRTA observatory at Palaiseau in the suburb of the greater Paris area

In order to evaluate the model and to perform sensitivity studies, the intensive observation period (IOP) number 13 from the ParisFog field campaign is simulated, because it is one of the best documented periods.

The ParisFog campaign is presented in Sect. 2, along with the measurements used to evaluate the model. Sect. 3 is devoted to the model description with particular emphasis on the treatment of fog microphysics. The modelling results and sensitivity analyses are presented in Sect. 4, and a discussion and conclusions are provided in Sect. 5.

2 Observations During the ParisFog Experiment

Data used in this study are measurements collected during the ParisFog field campaign, which took place during the winter 2006–2007 at the SIRTA observatory (48.713°N and 2.208°E). The site is located in a far suburb of Paris in what is considered a complex environment, which is composed of agricultural fields, wooded areas, a lake and building areas (Fig. 1). The objective of the ParisFog campaign was to understand the radiative, thermodynamic, dynamic and microphysical processes during the fog life cycle (Haeffelin et al. 2010). The full details of the ParisFog field project and the instrumentation are provided in Haeffelin et al. (2010), Bergot et al. (2008) and are available at http://sirta.ipsl.polytechnique.fr/parisfog/.

During ParisFog, over 100 fog and near-fog situations were documented to show the large variability of situations with predominant occurrences of radiation fog. Vertical profiles

Table 1 Instruments for particle size distribution measurements and their range of validity

Instrument	Size range (μm)
SMPS (scanning mobility particle size)	0.01–0.5
OPC GRIMM 1.109	0.004–3
OPC Pallas Welas 2000	0.04–40

of temperature, humidity and wind were measured along with near-surface temperature, humidity, longwave and solar radiation, aerosol size distribution and chemical composition in the surface layer. Instruments were deployed in three different zones in a 4 km^2 area. The dataset used in this study concerns zone 1 where a 30-m mast was equipped with standard weather sensors and sonic anemometers to monitor the vertical thermodynamic structure. Measurements were extended vertically by radiosonde profiles performed routinely at 0000 and 1200 UTC 15 km west of the SIRTA observatory. During IOPs, measurements were also made with radiosondes launched from the site every 3 h. Thermal and moisture soil conditions were monitored at 0.5-m depth and longwave and solar radiative fluxes and visibility were measured at the 2-m level. A ceilometer also provided a detailed description of the evolution of cloud and fog layers.

The particle size number spectra were documented in three size ranges with different equipment: a Scanning Mobility Particle Size (SMPS), an optical particle counter (OPC) GRIMM 1.109 and an OPC Pallas Welas (Table 1).

It should be noted that the fog-droplet number was collected in the upper diameter range (by Pallas Welas 2000) with a 20 % uncertainty on particle number per size bin. More recent measurements at the SIRTA observatory during fog events that included another OPC (FM100, Fog Monitor) seem to indicate that particles with radius $>4\,\mu$m are not accurately measured by the OPC Pallas Welas 2000. A detailed analysis of these data by Rangognio (2009) shows that it was difficult to distinguish wet aerosols from fog droplets. This was also mentioned by Gultepe et al. (2007, 2009) especially for polluted air masses. In addition, filter sampling permits the determination of the aerosol chemical composition, especially in terms of black carbon and sulphate.

Among the observed situations, we have selected the period of 18–19 February, which is one of the best documented.

3 Model Description

The atmospheric single-column model (SCM) used in this study is the one-dimensional (1-D) version of a three-dimensional (3-D) computational fluid dynamics (CFD) model *Code_Saturne* (Archambeau et al. 2004).

The SCM represents an isolated column of the atmosphere, and has 69 levels on the vertical grid with the lowest level at 2 m above the ground and the highest at 2,500 m. The full set of governing equations for the model is presented in the Appendix. We present here only the thermodynamic equations, which are derived from the conservation of moist static energy (Betts 1973), and in which the conservative variables are the liquid-water potential temperature and the total water specific stability given respectively by,

$$\theta_\mathrm{l} = \theta - \frac{L_\mathrm{v}\theta}{C_\mathrm{p}T} q_\mathrm{l}, \tag{1}$$

$$q_\mathrm{w} = q_\mathrm{v} + q_\mathrm{l}, \tag{2}$$

where θ_{l} (K) is the liquid-water potential temperature, θ (K) is the potential temperature, T (K) is the temperature, q_{w} ($\mathrm{kg\,kg^{-1}}$) is the total water specific humidity (sum of the specific humidity for water vapour q_{v} and liquid water q_{l}, with the latent heat of evaporation $L_{\mathrm{v}} = 2.5\,\mathrm{MJ\,kg^{-1}}$ and the specific heat capacity $C_{\mathrm{p}} = 1{,}005\,\mathrm{J\,kg^{-1}\,K^{-1}}$.

3.1 Fog Microphysics

The model used here is based on the two-moment warm-cloud bulk microphysical model, which was described and evaluated by Bouzereau et al. (2008); q_{l} is diagnosed from the predicted value of q_{w} by using a subgrid condensation scheme (Bouzereau et al. 2007),

$$\begin{array}{ll} q_{\mathrm{l}} = \alpha\,[q_{\mathrm{w}} - q_{\mathrm{s}}(T, P)] & \text{if } q_{\mathrm{w}} > q_{\mathrm{s}}(T, P) \\ q_{\mathrm{l}} = 0 & \text{if not,} \end{array} \tag{3}$$

where q_{s} is the water vapour specific humidity at saturation level and α is a coefficient that depends on the subgrid distribution law for specific humidity and temperature fluctuations ($\alpha = 1$ when the subgrid condensation scheme is inactive) (Bouzereau et al. 2007).

The total droplet number concentration N_{d} can be linked to the liquid water q_{l}; indeed, the number of cloud droplets as a function of their radius is represented by a log-normal size distribution, and reads

$$n_{\mathrm{d}}(r) = \frac{N_{\mathrm{d}}}{r\sqrt{2\pi}\sigma_{\mathrm{d}}} \exp\left[-\frac{(\ln(r/ro))^2}{2\sigma_{\mathrm{d}}^2}\right], \tag{4}$$

where r is the cloud droplet radius, N_{d} ($\mathrm{cm^{-3}}$) is the total droplet number concentration per unit volume, σ_{d} is the standard deviation of the distribution and r_0 is the median radius. By integrating the mass of droplets over the size spectrum, assuming this log-normal distribution, we then obtain a relationship between N_{d}, q_{l} and the mean volumetric radius r_{mv},

$$\rho\, q_{\mathrm{l}} = \frac{4}{3}\pi\, r_{\mathrm{mv}}^3 \rho_{\mathrm{w}} N_{\mathrm{d}}, \tag{5a}$$

with

$$r_{\mathrm{mv}} = r_0 \exp\left(\frac{3}{2}\sigma_{\mathrm{d}}^2\right). \tag{5b}$$

3.1.1 Nucleation

Nucleation is a key process that governs the number concentration of the fog droplets and depends on the supersaturation. Radiative cooling in the atmosphere is one of the main mechanisms driving the saturation in radiation fog. The model of Bouzereau et al. (2008) was, therefore, adapted in order to take this effect into account: a radiation term was added to the evolution equation of supersaturation $s = 1 - q_{\mathrm{v}}/q_{\mathrm{s}}$ (Abdul-Razzak and Ghan 2000),

$$\begin{aligned} \frac{\mathrm{d}s}{\mathrm{d}t} &= \underbrace{\left(\frac{\zeta L_{\mathrm{v}} g}{R_{\mathrm{a}} T^2 C_{\mathrm{p}}} - \frac{g}{R_{\mathrm{a}} T}\right)}_{\text{lifting}} W - \underbrace{\left(\frac{R_{\mathrm{a}} T}{\varsigma e_{\mathrm{s}}} + \frac{\varsigma L_{\mathrm{v}}^2}{p T C_{\mathrm{p}}}\right)}_{\text{latent heat release}} \frac{\mathrm{d}q_{\mathrm{l}}}{\mathrm{d}t} + \underbrace{\frac{\zeta L_{\mathrm{v}}}{\rho R_{\mathrm{a}} T^2 C_{\mathrm{p}}} \frac{\partial F_{\mathrm{rad}}}{\partial z}}_{\text{radiation}} \\ &= A_1 W - A_2 \frac{\mathrm{d}q_{\mathrm{l}}}{\mathrm{d}t} + A_3 \frac{\partial F_{\mathrm{rad}}}{\partial z}, \end{aligned} \tag{6}$$

where t (s) is the time, $\zeta = 0.622$ (rates of molecular weight of water to molecular weight of air), g is the acceleration due to gravity, R_a is the gas constant for dry air, W is the vertical air velocity, e_s (Pa) is the saturation vapour pressure water and F_rad the net radiative flux ($\mathrm{W\,m^{-2}}$).

As the primary source of cloud droplets, the nucleation process depends on many factors including the characteristics of aerosols (size and chemical composition). In order to take into account size distribution and chemical composition documented during ParisFog, the Abdul-Razzak and Ghan (2000) scheme for aerosol activation was used. This scheme uses three modes by superpositioning three log-normal aerosol distributions; the three modes used in this study are the Aitken mode, the accumulation mode and the coarse mode and are presented in detail in Sect. 4. The droplet number concentration at the maximum supersaturation s_max, is then given by

$$N_\mathrm{d}\left(s_\mathrm{max}\right) = \frac{1}{2}\sum_{i=1}^{3} N_{\mathrm{a}i}\left(1 - \mathrm{erf}\left[\frac{2\ln\left(s_i/s_\mathrm{max}\right)}{3\sqrt{2}\ln\sigma_{\mathrm{a}i}}\right]\right), \tag{7}$$

where $N_{\mathrm{a}i}$ is the total aerosol number concentration of mode i, s_i is the critical supersaturation of a particle with radius $r_{\mathrm{a}i}$ and the geometric mean radius of the aerosol mode i. Critical supersaturation can be calculated by using Köhler's theory (Pruppacher and Klett 1997); the maximum supersaturation s_max is given by

$$s_\mathrm{max} = \sum_{i=1}^{3}\frac{1}{s_i^2}\left[f_i\left(\frac{\varsigma}{\eta_i}\right)^{3/2} + g_i\left(\frac{s_i^2}{\eta_i + 3\varsigma}\right)^{3/4}\right], \tag{8}$$

with coefficients given in the Appendix.

3.1.2 Sedimentation and Deposition

Sedimentation is modelled by assuming a log-normal size distribution of droplets falling in a Stokes regime, in which the evolution of N_d and q_l are given by

$$\left(\frac{\partial N_\mathrm{d}}{\partial t}\right)_\mathrm{SED} = \frac{\partial}{\partial z}\int_0^\infty V_\mathrm{g}(r)\,n_\mathrm{d}(r)\,\mathrm{d}r = \frac{\partial}{\partial z}\left(N_\mathrm{d}\;V_\mathrm{g}\left(r_\mathrm{mv}\right)\;\exp(-\sigma_\mathrm{d}^2)\right), \tag{9}$$

$$\left(\frac{\partial q_\mathrm{l}}{\partial t}\right)_\mathrm{SED} = \frac{1}{\rho}\frac{\partial}{\partial z}\int_0^\infty V_\mathrm{g}(r)\frac{4\pi}{3}r^3 n_\mathrm{d}(r)\mathrm{d}r = \frac{1}{\rho}\frac{\partial}{\partial z}\left(\rho\;q_\mathrm{l}\;V_\mathrm{g}\left(r_\mathrm{mv}\right)\;\exp(5\sigma_\mathrm{d}^2)\right), \tag{10}$$

where V_g is the droplet fall velocity.

Here, $V_\mathrm{g}(r)$ is calculated as a function of the droplet-size radius

$$V_\mathrm{g}\left(r\right) = \rho g C_\mathrm{c} r^2 (4.5\mu_\mathrm{air})^{-1}, \tag{11}$$

where μ_air is the dynamic viscosity of the air, and $C_\mathrm{c} = 1 + \lambda_\mathrm{air}\left(1.257 + 0.4\exp\left(1.1r/\lambda_\mathrm{air}\right)\right)/r$ is the slip correction factor, called the Cunnigham correction factor, which accounts for non-continuum effects for small droplets (from 0.1 to 10 μm in diameter) and which depends on the mean free path of the air λ_air (Pruppacher and Klett 1997).

Fog deposition onto vegetation has long been recognized as an important factor in the water balance of ecosystems (Klemm and Wrzesinsky 2007). This process results from turbulent exchange of fog water between the air and the surface underneath and collection by the surface. In our model, the fog deposition flux, F_{dep}, is predicted from the simple inferential model equation

$$F_{\mathrm{dep}} = q_{\mathrm{l}} \frac{1}{R_{\mathrm{t}}} = q_{\mathrm{l}} V_{\mathrm{dep}}, \tag{12}$$

where V_{dep} is the deposition velocity and R_{t} is the total resistance against deposition, computed as the sum of aerodynamic (R_{aero}) and surface (R_{surf}) resistances between the ground surface and the first model grid level, viz.

$$R_{\mathrm{aero}} = \frac{\ln(z_1/z_0) - \psi_{\mathrm{h}}}{\kappa u_*}, \tag{13a}$$

$$R_{\mathrm{surf}} = \frac{1}{\varepsilon_0 u_* (E_{\mathrm{imp}} + E_{\mathrm{int}})}, \tag{13b}$$

where z_1 is the height at which the deposition velocity is evaluated, z_0 is the aerodynamic roughness length, ψ_{h} is a stability function, κ is the von Karman constant, u_* is the friction velocity, and $\varepsilon_0 = 3$ is an empirical constant for all types of land. E_{imp} and E_{int} are collection efficiencies for impaction by inertia and interception, respectively (Zhang et al. 2001),

$$E_{\mathrm{imp}} = \left(\frac{St}{St + 1.5}\right)^2, \tag{14a}$$

with

$$St = \frac{V_{\mathrm{g}} u_*}{0.01 g}, \tag{14b}$$

$$E_{\mathrm{int}} = 2\left(\frac{r_{\mathrm{mv}}}{0.01}\right). \tag{14c}$$

The collection by Brownian motion of fog droplets is neglected because its effect is only significant for very small particle diameters (<0.1 μm) (Ritter et al. 2008). If sedimentation is taken into account, a new bulk velocity is computed as the sum of V_{g} and V_{dep} at the lowest level and is then used to estimate F_{dep}.

3.2 Turbulence Closure

The turbulence closure is first-order where the turbulent kinetic energy (TKE) and the dissipation rate ε are diagnosed by using the Kolmogorov approximation and a steady-state hypothesis for the TKE equation, which results in a balance between the production and dissipation terms (Musson-Genon 1995). In this closure, the turbulent exchange coefficients are computed as a function of the mixing length and the bulk Richardson number R_i: $K_{\mathrm{m}} = |\partial U/\partial z| l^2 F_{\mathrm{m}}(R_i)$ for momentum and $K_{\mathrm{h}} = |\partial U/\partial z| l^2 F_{\mathrm{h}}(R_i)$ for scalars, where U is the horizontal wind speed, $l = \kappa z(1 + \kappa z/l_{\mathrm{c}})$ with $l_{\mathrm{c}} = \Delta z/2.5$, $F_{\mathrm{m}}, F_{\mathrm{h}}$ are functions depending on thermal stratification, in which the effect due to water phase changes is considered (Musson-Genon 1995).

3.3 Radiation

The longwave radiation transfer equation is solved by using the emissivity approximation; gas absorption is computed for water vapour and its dimers, carbon dioxide and ozone. The effect of clouds is described by transmission functions for liquid water overlapping absorption by gases by means of an extinction coefficient $K_{\mathrm{ext}} = 1.66 q_{\mathrm{l}}/(\rho_{\mathrm{w}} r_{\mathrm{e}})$, where

$r_{\mathrm{e}} = \int r^3 \mathrm{d}r / \int r^2 \mathrm{d}r = r_{\mathrm{mv}} \exp(\sigma_{\mathrm{d}}^2)$ is the equivalent radius of the droplet-size distribution for a totally absorbing medium (scattering is neglected). The cloud fraction, as determined in our subgrid condensation scheme, is calculated from Bougeault (1985).

For solar radiation, a two-band model (0.2–0.7 and 0.7–4.0 μm) of Lacis and Hansen (1974) scheme is used but with substantial improvements. The "δ Eddington" approximation with the correction of Joseph et al. (1976) is used for the two-stream method. Scattering is treated by using the adding method. Clouds are defined by their liquid water content (LWC), cloud fraction and droplet-size spectrum that permit the determination of a prognostic effective radius r_{e}.

For the cloud droplet single-scattering albedo, we can take into account the pollutant concentration following Sandu et al. (2005); it is parametrized as a function of the cloud droplet diameter, the black carbon volume fraction, the wavelength and the effective refractive index. The aerosol single-scattering albedo depends on the scattering aerosol optical thickness ($\mathrm{AOT_{scat}}$) and the total aerosol optical thickness ($\mathrm{AOT_{tot}}$): $\omega_{\mathrm{a}} = \mathrm{AOT_{scat}}/\mathrm{AOT_{tot}}$, following Tombette et al. (2008), where ω_{a} takes the value 0.84 given by Leighton (1980). Cloud fraction is included in addition to the original adding method with the k-distribution method for water vapour/liquid overlap.

3.4 Nudging

In order to take into account the larger scale meteorological conditions, the model variables are nudged at every timestep to observational data or operational analyses. Thus, the prognostic equations of the model contain an additional term in the form,

$$\frac{\partial X}{\partial t} = M(X) + C_n \left[Y(t) - X \right], \tag{15}$$

where X is the prognostic variable, $M(X)$ represents the different terms of the equation, C_n is a nudging coefficient, and $Y(t)$ is the large-scale meteorological driving field that can be estimated from observations or using the fields from a numerical prediction model. The driving fields are determined by using the observations available during the IOP13: near-surface observations (2, 10 and 30 m) and radiosonde data for upper air levels. The process of transforming data from observations at irregularly spatio-temporal points into data at regularly distributed points on the model grid is based on an objective analysis technique (Cressman 1959).

3.5 Boundary and Initial Conditions

At the top of the model, a null flux condition is imposed. At the surface (or more precisely at $z = z_0$), a rough-wall boundary condition is applied. The evolution of land-surface temperature T_{surf} and humidity q_{surf} can be treated in our model through two different methods with reasonable results: (1) the force-restore method and (2) the atmospheric surface-layer method.

(1) The first one has been employed with considerable success in numerical weather prediction models to estimate diurnal variations in the land-surface temperature by using an energy balance equation at the Earth surface (Deardorff 1978).

(2) The second method (Musson-Genon et al. 2007), based on the Obukhov similarity theory, presents a technique for reconstruction of T_{surf} and q_{surf} evolutions based on measurements of wind speed, temperature, and humidity at two different levels. This temporal dataset replaces the land-surface atmospheric model and is imposed at the land surface as

Table 2 Aerosol size distribution characteristics at 2100 UTC during IOP 13 used in the control simulation

	Aitken mode	Accumulation mode	Coarse mode
N_a (cm^{-3})	8,700	8,300	1,000
R_a (µm)	0.0165	0.055	0.4
σ_a	1.57	1.59	1.3

Table 3 Aerosol chemical composition, percentage representing the mass fraction of each compound contained in the aerosol

Composition	Sulphate	Nitrate	Soot	Organic
Percentage (%)	25	20	16.4	38.6

external parameters, and can be considered as a land-surface boundary-layer forcing condition. The advantage of using this method is that one can test physical parametrizations without having to use additional modelling of the land–atmosphere interaction.

The initial conditions (temperature, humidity and wind) were obtained by an objective analysis scheme from the radiosonde and 30-m mast data, as described above.

4 Results

4.1 Control Simulation

The control simulation with reconstructed T_{surf} and q_{surf} is initialized at 1200 UTC 18 February 2007 and covers the period until 1200 UTC 19 February 2007 when the fog has lifted into a stratus cloud layer. Meanwhile, the SCM was operated in "nudging mode", where the temperature, humidity and wind profiles were nudged to the observed analyzed profiles (see above) using a relaxation time coefficient C_n ($10^{-4}\,\mathrm{s}^{-1}$ near the ground, $10^{-3}\,\mathrm{s}^{-1}$ at 2,500 m). The initialization of the cloud-droplet activation spectrum is performed through a fitting procedure determining the parameters of log-normal laws by using the aerosol size spectrum (Table 2) and chemical composition (Table 3) measured at 2100 UTC 18 February 2007 (Rangognio 2009).

The number of aerosol particles in the coarse mode is fixed at 1,000 cm^{-3}, close to the value measured by the Pallas Welas (2000) just before fog appearance. The standard deviation for cloud droplets is fixed at 0.26, which is a realistic value for boundary-layer clouds (Cohard et al. 1998; Bouzereau et al. 2007). The visual range (*VIS*) is calculated with the recent formulation given by Gultepe et al. (2006), in which both the LWC (q_{l}) and droplet number (N_{d}) are used,

$$VIS = 1.002(\rho q_{\mathrm{l}} N_{\mathrm{d}})^{-0.6473}. \tag{16}$$

4.1.1 Weather Conditions Precluding Fog Appearance

The day of February 18 2007 was characterized by high pressure over northern France after ten days of perturbed weather; it results in clear sky and light wind over the SIRTA area during the day (Fig. 3a) with a maximum temperature around 15°C (Fig. 3b) and $VIS > 3{,}000$ m due

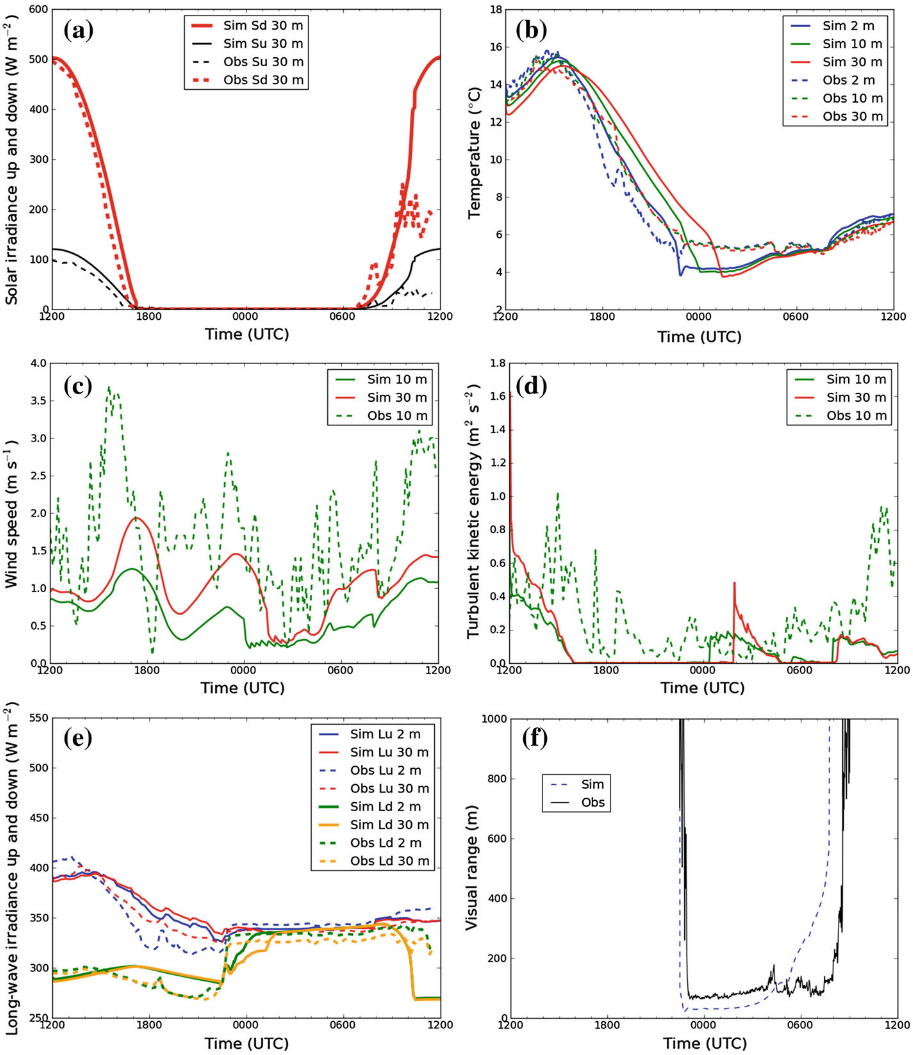

Fig. 2 Comparison of the temporal evolution of simulated (Sim) and observed (Obs): **a** downward solar radiation irradiance at 30 m; **b** temperature at 2, 10 and 30 m; **c** wind speed at 10 and 30 m; **d** TKE at 10 and 30 m; **e** downward longwave irradiance (Ld) and upward longwave irradiance (Lu) at 2 and 30 m; **f** visual range at 2 m

to a moderate aerosol load. At sunset (1600 UTC), when the surface layer becomes stable, the wind speed significantly increases, with the wind direction turning eastward (Fig. 3c) and the advection of aerosols from the Paris area. Increase in wind speed is simulated, but the wind speed is significantly underestimated and timing is delayed ≈1 h compared to observations. This is partly due to local heterogeneities, which are not taken into account in the 1-D approach, notably the channelling by the forest canopy to the north of the instrumented area at the 10-m level (Zaïdi et al. 2012). From 1800 UTC to 2200 UTC, the 2-m temperature decreases even if a short cloud passage induces a small increase in temperature and both downward and upward longwave radiation fluxes (Fig. 2e). This phase of clear-sky cooling

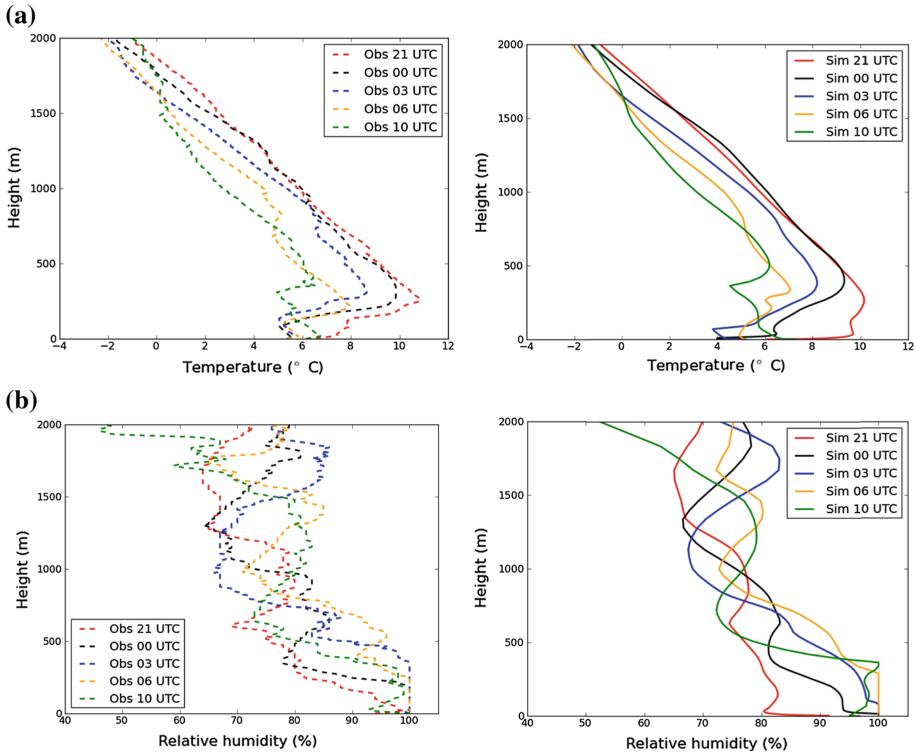

Fig. 3 Comparison between observed (Obs, *left*) and simulated (Sim, *right*) at 2100, 0000, 0300, 0600, 1000 UTC: **a** vertical temperature profiles; **b** vertical relative humidity profiles

near the surface is rather well reproduced with a ground forcing deduced from observations. Nevertheless we can note insufficient simulated cooling in the stable layer (Fig. 2b). In fact, a stable layer is simulated even if the cooling is too weak. The problem is that measurements show a well-mixed thermal layer between 10 and 30 m, which is not reproduced in our simulation. The reason could be turbulent mixing at these levels (Fig 2d), partly due to the complex heterogeneities of the site and/or a local cold-air advection as suggested by the temperature profile at 2100 UTC (Fig. 3a).

4.1.2 Fog Formation

The fog appears close to the ground at approximately 2230 UTC. This formation is characterized by a strong decrease in visual range (Fig. 2f) at 2 m with rapid variation in time from 1,000 to less than 100 m. At the same time, we observe very low wind speed and, TKE at 10 m (Fig. 2c and 2d). The deepening of the fog layer is rapid in the first 30 m associated with a well-mixed layer between 2 and 30 m (Fig. 2b) and a rapid increase of turbulence and wind speed (Fig. 2c, d). This deepening is also characterized by a strong increase of both upward and downward longwave radiation fluxes (Fig. 2e). The time of formation is well predicted at the 2-m level (Fig. 2f) but not the rapid deepening. In the simulation, this deepening occurs 1 and 2 h too late at respectively 10 and 30-m, due to the overestimated temperature at these levels just before fog appearance. Turbulent intensity is clearly underestimated but the TKE peak at 10 m occurs when the fog layer reaches this level due to the destabilization of the thermal structure by longwave radiation cooling at the fog top.

4.1.3 Fog Development

After 0000 UTC, the fog layer deepens from $z = 200$ to 300 m as seen in the temperature and humidity profiles at 0000 and 0300 UTC (Fig. 3a, b). This deepening of the fog layer between 0300 UTC and 0600 UTC is probably partly due to a significant cooling of the upper layers above 400 m (Fig. 3a). This phase is followed by a slight subsidence between 0300 UTC and 0600 UTC. These two phases are not well reproduced in the simulations, for which the depth of the fog layer increases regularly from 50 to 300 m between 0000 UTC and 0600 UTC. This can be explained by a fine balance between subsidence, entrainment and detrainment at the top of the fog layer due to turbulent mixing linked to the longwave radiation cooling in the presence of wind shear that is not so well represented in our modelling.

4.1.4 Fog Decay

The dissipation phase begins at 0840 UTC with fog lifting from the ground, after which the fog layer evolves into low stratus still present at the beginning of the afternoon. The model simulates correctly the fog lifting but the simulated stratus that appears afterwards disappears at 1030 UTC.

If we look at the microphysical evolution during the life cycle of the simulated fog, we observe that the number of fog droplets is well mixed in the vertical with a total number of fog droplets of approximately 800 cm^{-3} (Fig. 4a). This value depends on the number of aerosol particles. On the contrary, at a given time, the LWC varies in the vertical, with a maximum occurring at the top of the fog layer where the longwave cooling is stronger (Fig. 4b), as observed by Gultepe et al. (2009). The fog-droplet size spectrum (Fig. 4c) is rather constant during both formation and development phases. A net reduction of the droplet radius occurs between 0300 UTC and 0500 UTC when $q_1 > 0.1\,\mathrm{g\,kg}^{-1}$ associated with fog elevation and between 0500 UTC and 0700 UTC during the dissipation phase due to evaporation process.

Generally the model with the options initially chosen simulates rather well the fog evolution, but the results obtained are sensitive to many processes, such as turbulent closure, forcing at the ground, the nudging coefficient and the microphysics of fog droplets.

For turbulent closure, the parametrization presented by Musson-Genon (1987) is used as described in the original paper. The equations of change for TKE and its dissipation have also been used but they lead to greater q_1 (0.6 g kg^{-1}) at the top of the fog layer due to a sudden decrease in turbulence at these levels. For the ground forcing, a force-restore method has been tested with an adjusted set of local parameters, which gives satisfying results but does not match as closely the observations as does the atmospheric surface-layer method (results not presented here).

The nudging coefficient has been chosen in order to be small close to the surface (10^{-4} s^{-1}) and large in the upper layer (10^{-3} s^{-1}). The results are sensitive to this coefficient. A value that is too large could disrupt the balance of the different physical processes modelled (especially the saturation) and a value that is too small does not allow sufficient forcing towards the observations. For example, it is very difficult to obtain realistic results during a 24-h time period without forcing to the synoptic conditions. The formulation retained in our simulations gives a nudging coefficient value of $3 \times 10^{-4}\,\mathrm{s}^{-1}$ at 500 m, which is the value

Fig. 4 Temporal evolution of: **a** the simulated total number of fog droplets at different levels; **b** the simulated LWC in g kg^{-1}; **c** the fog-droplet size spectrum simulated at 2 m between 2300 UTC and 0700 UTC

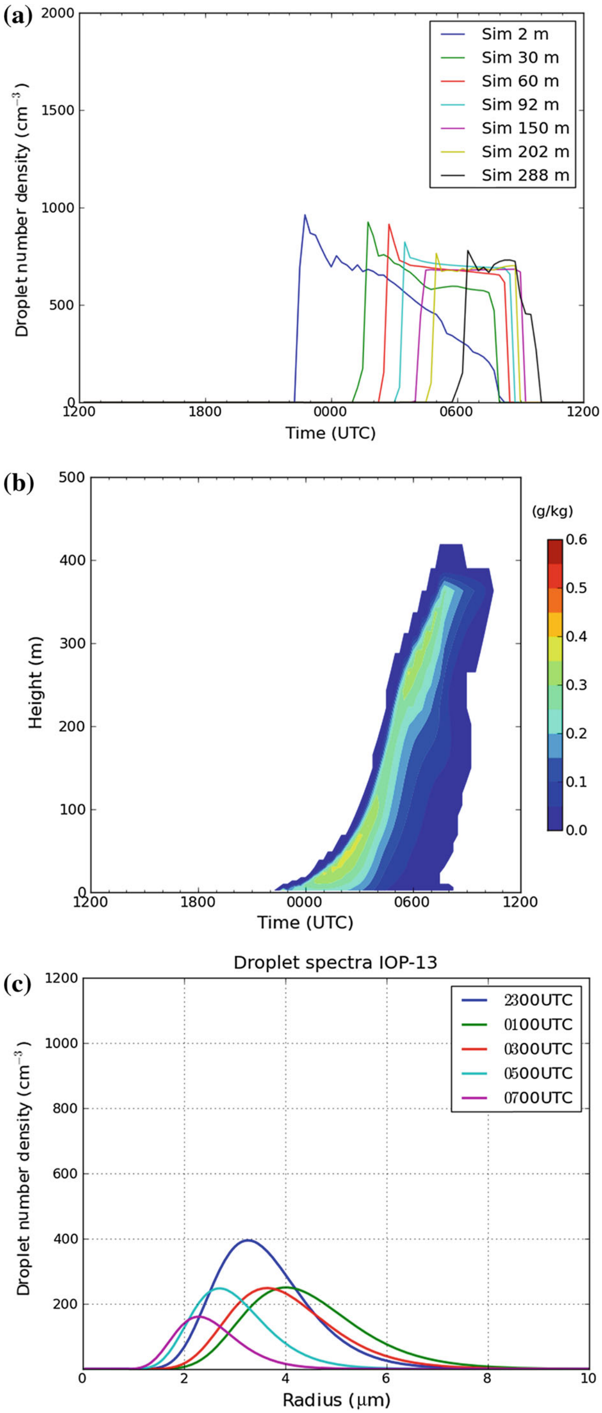

used in version 3 of the WRF model analysis nudging system (Skamarock et al. 2008). A sensitivity analysis study shows that the impact is low for values varying from 0.8×10^{-4} to $1.2 \times 10^{-4}\,\mathrm{s}^{-1}$.

4.2 Sensitivity Study on the Microphysics of Fog Droplets

Only a few models have an explicit description that allows analysis of all the interactions between the microphysics of fog and the other predominant processes governing its evolution. Therefore, we perform here a sensitivity study on the microphysics of fog droplets:

The microphysics of fog droplets (droplet number concentration and size distribution) interact with the fog thermodynamics through essentially two processes:

(i) The droplet sedimentation that leads to a redistribution of the LWC in the vertical. The gravitational settling of fog droplets is linked to the mean volumetric radius through Stokes law (Eq. 11).
(ii) The radiation cooling/heating where the extinction coefficient depends explicitly on the droplet-size distribution both for longwave and solar radiation.

In our simple modelling approach, the fog microphysics is driven by

- the nucleation process, which essentially governs the number concentration of droplets when fog appears. The nucleation scheme that we used was modified to take into account radiation cooling in the determination of the supersaturation. With the aerosol concentration characteristics retained for our simulations, the droplet activation depends essentially on the number of wet aerosol particles present in the coarse mode.
- the characteristics of the log-normal distribution used for droplets. The standard deviation σ_d is a fixed parameter of the log-normal distribution and is used in the determination of the equivalent radius for radiation and of the mean volumetric radius for sedimentation.

In order to perform sensitivity analysis on these aspects, we used the nucleation scheme of Abdul-Razzak and Ghan (2000) with two different values for the number of wet aerosols $N_\mathrm{a} = 1{,}400\,\mathrm{cm}^{-3}$ (case 1) and $N_\mathrm{a} = 600\ \mathrm{cm}^{-3}$ (case 2), the value on the control run being $N_\mathrm{a} = 1{,}000\,\mathrm{cm}^{-3}$. For the same value of q_1, these values lead to different mean volumetric radii for droplet through Eqs 5.

For those two cases, simulations are performed using, (a) nucleation without sedimentation and deposition, (b) nucleation with sedimentation but without deposition, (c) nucleation with sedimentation and deposition.

(*a*) *Nucleation without sedimentation and deposition*

For the same value of σ_d ($\sigma_\mathrm{d} = 0.26$), case 1 leads to the formation of a large number of droplets with $r_\mathrm{mv} \approx 4\,\mu\mathrm{m}$. Case 2 leads to a smaller number of droplets and consequently greater r_mv (Fig. 5).

For simulations without sedimentation processes, comparisons between case 1 and case 2 for the temporal evolution of the LWC and droplet-size distribution are presented in Figs. 5 and 6, respectively. Case 2 gives a cooling rate slightly lower than case 1, but this difference is too small to have any effect on the evolution of the LWC in the fog layer (Fig. 6).

One can note that the time of fog formation is the same for both cases. In fact the time of fog formation is more influenced by temperature and specific humidity through the saturation pressure vapour than by the aerosol number concentration. Indeed, in such a type of polluted situation in the greater Paris area, there are always sufficient aerosols to form fog droplets. This low dependence on aerosol number concentration was also found by Rangognio et al. (2009), who simulated the same case with the meso-NH model.

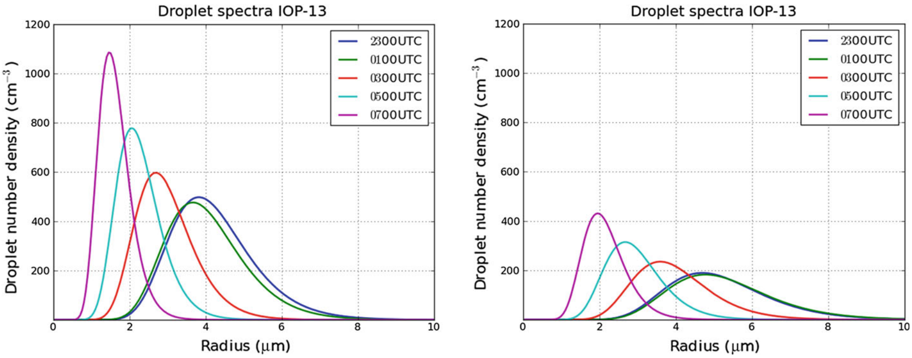

Fig. 5 Effect of the number of aerosol particles: comparison of fog-droplet size spectra for case 1 with $N_a = 1{,}400\,\mathrm{cm}^{-3}$ (*left*) and case 2 with $N_a = 600\ \mathrm{cm}^{-3}$ (*right*) in the case where sedimentation and deposition are not taken into account

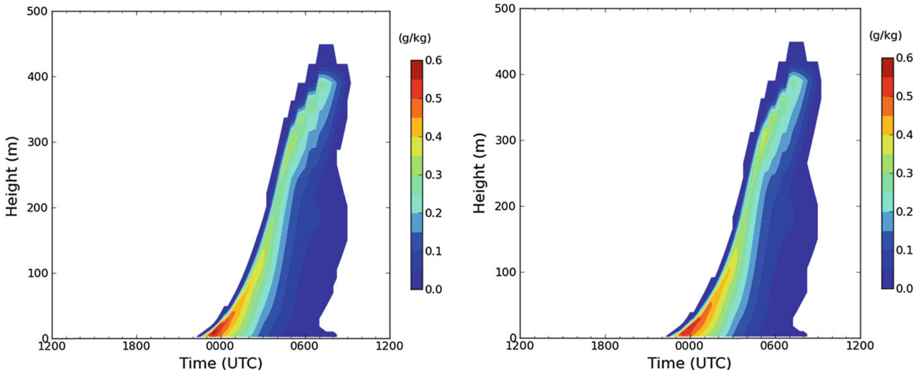

Fig. 6 Effect of the number of aerosol particles: comparison of the temporal evolution of the LWC for case 1 with $N_a = 1{,}400\,\mathrm{cm}^{-3}$ (*left*) and case 2 with $N_a = 600\ \mathrm{cm}^{-3}$ (*right*) in the case where sedimentation and deposition are not taken into account

(*b*) *Nucleation with sedimentation but without deposition*

By taking into account sedimentation (Fig. 7), these results are greatly modified for both cases. In that case, the maximum LWC is lower (0.45 $\mathrm{g\ kg^{-1}}$ instead of 0.6 $\mathrm{g\ kg^{-1}}$) and the vertical development of the fog layer is delayed by 1 h in case 1 and 2 h in case 2. The sedimentation effect, keeping liquid water close to the ground, is more pronounced for case 2 where r_{mv} is larger. In that case, the development of the fog layer in the vertical is too slow and gives greater values for the LWC at the top of the fog layer ($\approx$ 300 m) at 0600 UTC. This results in maintaining a stratus layer from 1000 UTC until 1200 UTC as can be seen in Fig. 8 (right). For the dissipation at the ground, the results for case 1 and case 2 are quite similar and the visual range increases rapidly at 0830 UTC, at practically the same time in both cases (Fig. 8). The transition to a stratus layer is well simulated by case 2 with a correct cloud-base height $\approx$ 250 m at 1200 UTC compared to that deduced from the backscattering signal obtained from ceilometer measurements (Fig. 9). In this figure, we see that the dissipation of the fog layer begins at the surface at 0830 UTC and lifts into a stratus layer, which dissipates at 1430 UTC, confirming that a stratus layer is still present at 1200 UTC.

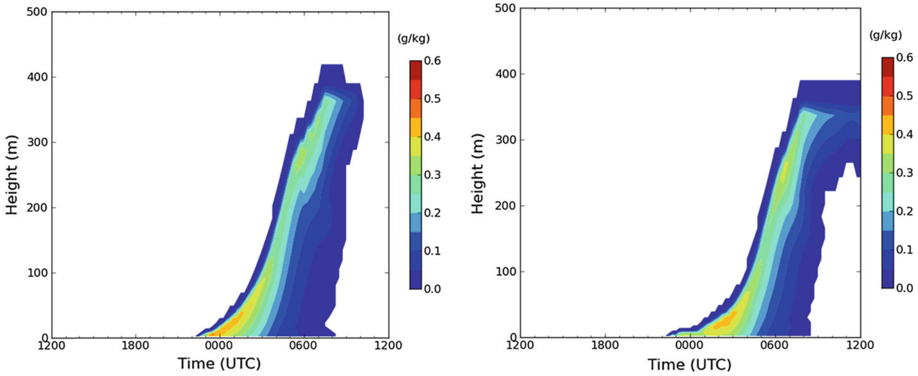

Fig. 7 Effect of the number of aerosol particles: comparison of the temporal evolution of the LWC for case 1 with $N_\mathrm{a} = 1{,}400\,\mathrm{cm}^{-3}$ (*left*) and case 2 with $N_\mathrm{a} = 600\ \mathrm{cm}^{-3}$ (*right*) in the case where sedimentation is taken into account

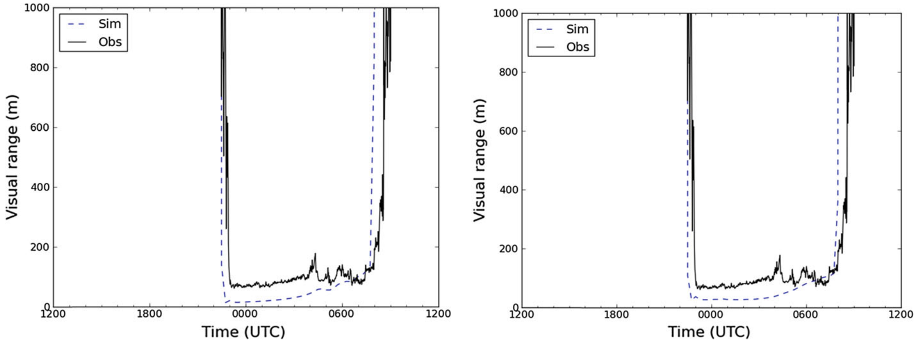

Fig. 8 Effect of the number of aerosol particles: comparison of the temporal evolution of the visual range for case 1 with $N_\mathrm{a} = 1{,}400\,\mathrm{cm}^{-3}$ (*left*) and case 2 with $N_\mathrm{a} = 600\ \mathrm{cm}^{-3}$ (*right*) in the case where sedimentation is taken into account

In comparison to sensitivity study a), the time of fog formation does not change for both cases. Case 2 is also in better agreement with observations for the downward radiation fluxes at 2 and 30 m, both in the solar and longwave domains, as can be seen in Figs. 10 and 11.

Note that the same results could be obtained with case 2 and case 1 by using a smaller value for σ_d in case 2 or a greater value for σ_d in case 1. The sedimentation term for the LWC is strongly dependent on both σ_d and the droplet radius (see Eq. 10) and, this effect is non-linear. When the droplet radius is less than 4 μm, the sedimentation effect is low but it increases significantly with a greater radius. We can see that, if the time of fog formation is well established, the fog evolution depends significantly upon the choices made for the microphysical parametrizations.

(*c*) *Nucleation with sedimentation and deposition*

As expected, taking into account deposition velocity diminishes the LWC close to the ground in the fog formation phase but has a low impact on further development (Fig. 12). Nevertheless, in the dissipation phase, the cases including deposition processes lead to a more progressive increase of the visual range, the fog layer disappearing a little too early for both case 1 and case 2 (Fig. 13). Nevertheless, visibility at 2 m seems to be systematically too low during early and mature fog stages. This could be due to larger values for the droplet

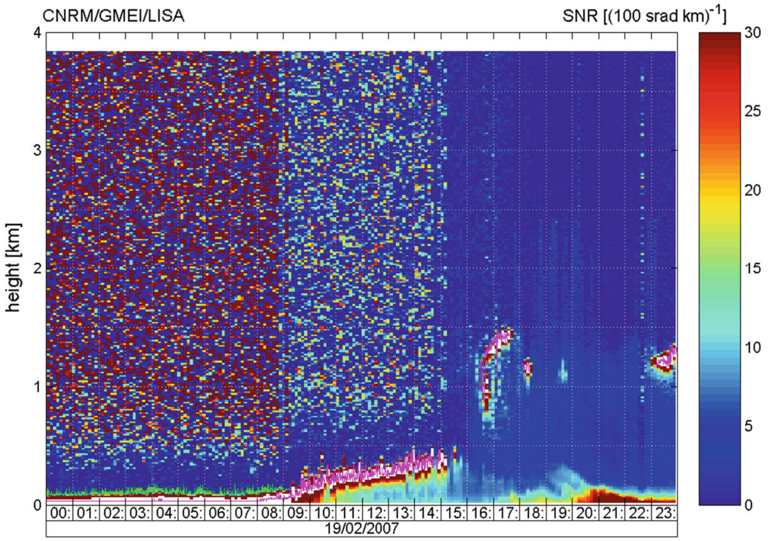

Fig. 9 The temporal evolution of the ceilometer backscattering signal

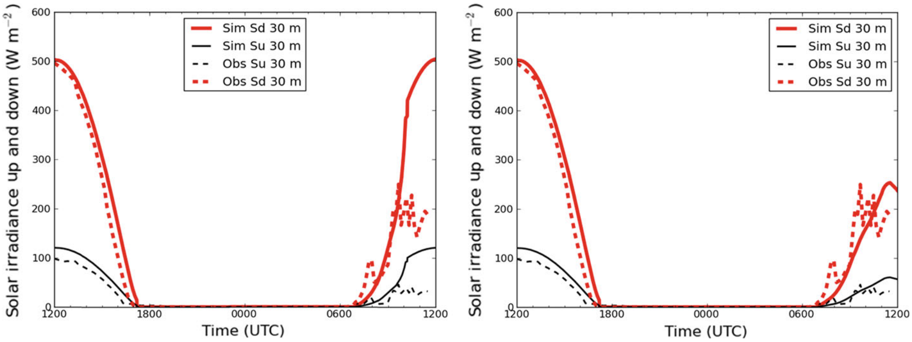

Fig. 10 Effect of the number of aerosol particles: comparison of the temporal evolution of simulated (Sim) and observed (Obs) downward solar irradiance (Sd) and upward solar irradiance (Su) at 2 and 30 m for case 1 with $N_a = 1{,}400\,\text{cm}^{-3}$ (*left*) and case 2 with $N_a = 600\ \text{cm}^{-3}$ (*right*)

number concentrations, partly due to the lack of large droplets, which are not well simulated with our semi-spectral model using only one log-normal distribution. On the other hand, during the dissipation phase, visibility could be too large because wet aerosols are not taken into account in the formulation of visibility with the Gultepe et al. (2006) parametrization, as revealed by Elias et al. (2009) and mentioned by Rangognio et al. (2009).

5 Conclusions and Perspectives

A SCM including simple microphysical parametrizations was used to simulate a radiation fog event during the ParisFog experiment, which took place in the winter of 2006–2007 in a southern suburb of Paris, France.

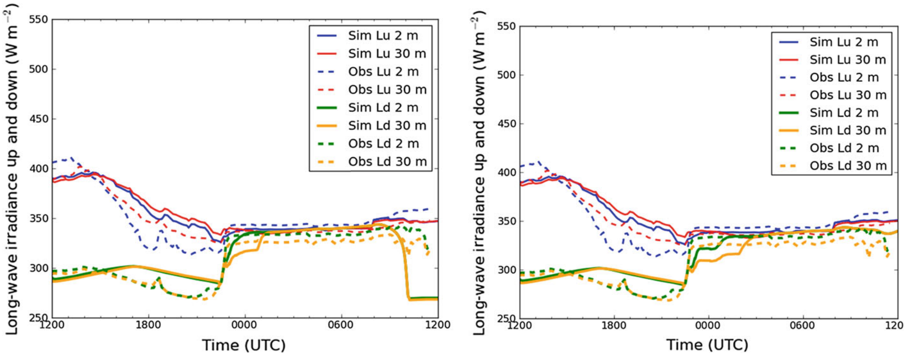

Fig. 11 Effect of the number of aerosol particles: comparison of the temporal evolution of simulated (Sim) and observed (Obs) downward longwave irradiance (Ld) and upward longwave irradiance (Lu) at 2 and 30 m for case 1 with $N_a = 1{,}400\,\mathrm{cm}^{-3}$ (*left*) and case 2 with $N_a = 600\ \mathrm{cm}^{-3}$ (*right*)

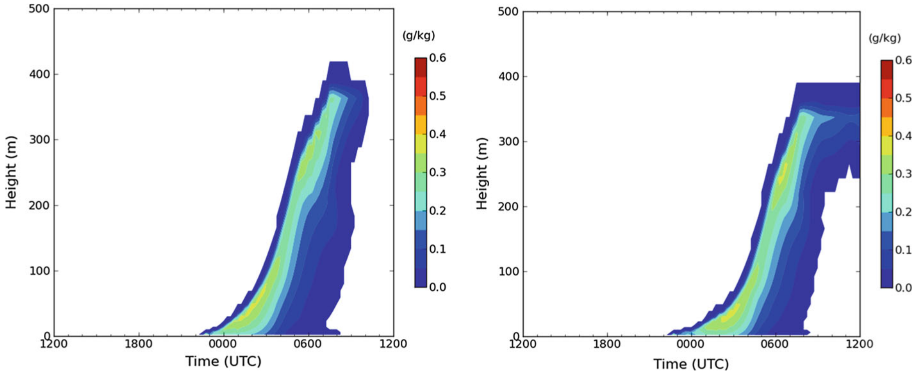

Fig. 12 Effect of the number of aerosol particle: comparison of the temporal evolution of the LWC for case 1 with $N_a = 1{,}400\,\mathrm{cm}^{-3}$ (*left*) and case 2 with $N_a = 600\ \mathrm{cm}^{-3}$ (*right*) in the case where both sedimentation and deposition are taken into account

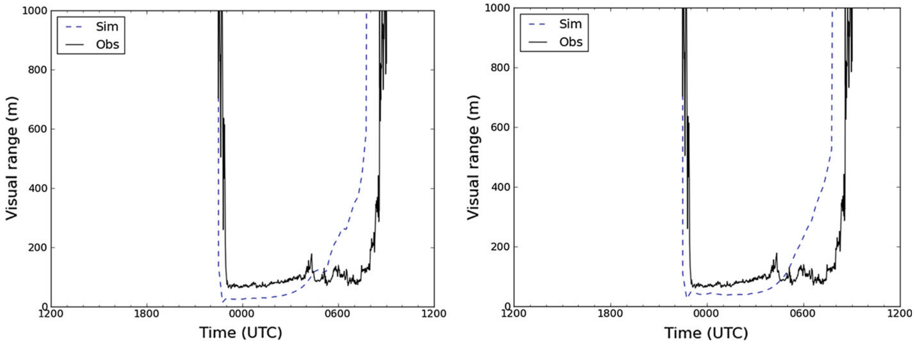

Fig. 13 Effect of the number of aerosol particles: comparison of the temporal evolution of the visual range for case 1 with $N_a = 1{,}400\,\mathrm{cm}^{-3}$ (*left*) and case 2 with $N_a = 600\ \mathrm{cm}^{-3}$ (*right*) in the case where both sedimentation and deposition are taken into account

This study was conducted for one of the better documented fog situations (IOP13), although measurements of the droplet-size distribution were not accurate enough. In order to have realistic simulations that allow us to achieve sensitivity tests under good conditions, the surface temperature and humidity were obtained from observations. Assimilation of upper air radiosounding data was achieved by using a nudging technique in the vertical direction. Under these conditions, the control simulation compares satisfactorily with measurements obtained during the IOP 13 of the ParisFog experiment.

With this control version, sensitivity tests were performed to study the role of microphysical processes and characteristics (nucleation, radiative cooling/heating, sedimentation, deposition) during the entire life cycle of a fog event. The sensitivity analysis was conducted by varying the wet aerosol number concentration in the coarse mode, which dominates the formation of fog droplets. Main conclusions are:

- The droplet-size distribution has a small influence on the role of longwave and shortwave radiation in the fog development and its LWC.
- As expected, sedimentation is a key parameter in the fog evolution and the droplet-size distribution has a strong influence, especially during the dissipation phase associated with the transition to a stratus layer. This is specifically due to the strong dependence of sedimentation velocity on the droplet radius when it exceeds a critical value.
- Deposition to surfaces seems to have some effect on the fog-droplet concentration in the layer near the ground and consequently on atmospheric visibility.
- On the simulated case, the time of fog formation seems to be independent of the aerosol number concentration; this result confirms the results of Rangognio et al. (2009) with the meso-NH model on the same case.

These results illustrate the need to better document microphysics in a future experimental design. For example, one should include other droplet OPC, FM-100 (Fog Monitor), PVM Gerber (Particulate Volume Monitor) at different vertical levels to obtain independent experimental estimations of the LWC and droplet-size distribution. In addition, optical extinction measurements could be useful in order to close the budget of liquid water and aerosol content as done by Elias et al. (2009).

With detailed measurements of aerosols (distribution in size and chemical composition), it will be possible to obtain a more comprehensive evaluation of the nucleation parametrization even if it seems difficult to experimentally determine supersaturation. This type of measurement is now available at the SIRTA observatory and analyses are currently being performed in order to use such data for model evaluation.

Despite this lack of microphysical experimental information, the semi-spectral approach used here is based on some simplifications.

- First, it appears that two modes are often present on fog-droplet size distribution that cannot be represented with a single log-normal distribution. It seems that if some droplet-size distribution were characterized by a continuous decrease of droplet concentration with size, many studies show mostly bi-modal droplet-size distributions (Gultepe et al. 2009). These two modes cannot be represented by the monomodal distribution used in this study.
- Second, sedimentation is very sensitive to the standard deviation of the log-normal distribution σ_{d} and to the radius of fog droplets above a certain threshold. Therefore, the use of a single log-normal distribution with a constant value for the standard deviation of the distribution seems too simplistic.

A better solution could be to have an explicit description of the size distribution with a sectional approach as used for example by Brown (1980). This technique is computationally expensive but could be attractive in a 1-D approach coupled with a mesoscale model. For 3-D calculations, it seems more adequate to keep a parametric approach but the use of two (or three) log-normal distributions with variable σ_d could be a significant improvement, as done for example in some aerosol models (Seigneur et al. 1986; Zhang et al. 1999; Sartelet et al. 2005), with, at least, a specific log-normal function representing the nucleation mode, and another representing the sedimentation mode.

This analysis of the microphysical aspects should not hide the important role of turbulence mixing, and large-eddy simulations that could be performed in order to better investigate this aspect, especially in 3-D simulations taking into account all spatial heterogeneities characterizing the environment of the SIRTA area such as forest, grass, water and building areas (Zaïdi et al. 2012). In addition, radiation processes have to be investigated in order to identify the role of aerosols in longwave cooling and that of their chemical composition in a modification of the optical properties of fog droplets that will be important for fog dissipation by solar radiation.

Acknowledgments This study is part of the Ph.D. thesis of Xiaojing Zhang, as part of the ParisFog project supported by Institut Pierre-Simon Laplace (IPSL), Centre National de Recherches Météorologiques (CNRM), and the Atmospheric Environment Teaching and Research Center (CEREA). We gratefully thank all the people who have worked during the ParisFog campaign. Special thanks are also due to Thierry Bergot, Jérôme Rangognio, Martial Haeffelin and Jean-Charles Dupont for useful discussions and comments during the Ph.D. thesis of Xiaojing Zhang and to the unknown reviewer for their very detailed comments.

Appendix

Model Equations

Dynamic Equations

The dynamic equations are written as

$$\frac{\partial U}{\partial t} = \frac{\partial}{\partial z}\left(K\frac{\partial U}{\partial z}\right) + C_n\left(U - U_{\mathrm{obs}}\right), \tag{17}$$

where U is the horizontal wind component, K is the wind exchange coefficient, C_n is the nudging coefficient (inverse of relaxation time: $1/\tau_n$), U_{obs} is the driving wind field derived from observations.

Thermodynamic Equations

Prognostic equations for the liquid-water potential temperature, θ_{l}, and for the total specific cloud water content q_{w} are

$$\rho\frac{\partial \theta_{\mathrm{l}}}{\partial t} = \frac{\partial}{\partial z}\left[\left(\frac{\lambda_{\mathrm{c}}}{C_{\mathrm{p}}} + \frac{\mu_{\mathrm{t}}}{P_{\mathrm{r}}}\right)\frac{\partial \theta_{\mathrm{l}}}{\partial z}\right] - \frac{\theta}{TC_{\mathrm{p}}}\frac{\partial F_{\mathrm{rad}}}{\partial z} - \rho\frac{L_{\mathrm{v}}\theta}{TC_{\mathrm{p}}}\left(\frac{\partial q_{\mathrm{l}}}{\partial t}\right)_{\mathrm{SED}} + \rho C_n(\theta_{\mathrm{l}} - \theta_{l_{\mathrm{obs}}}), \tag{18}$$

$$\rho\frac{\partial q_{\mathrm{w}}}{\partial t} = \frac{\partial}{\partial z}\left[\left(\frac{\lambda_{\mathrm{c}}}{C_{\mathrm{p}}} + \frac{\mu_{\mathrm{t}}}{P_{\mathrm{r}}}\right)\frac{\partial q_{\mathrm{w}}}{\partial z}\right] - \rho\left(\frac{\partial q_{\mathrm{l}}}{\partial t}\right)_{\mathrm{SED}} + \rho C_n(q_{\mathrm{w}} - q_{w_{\mathrm{obs}}}), \tag{19}$$

where ρ is the air density, λ_{c} is the thermal diffusivity, μ_{t} is the turbulent viscosity, P_{r} is the turbulent Prandtl number, F_{rad} is the vertical divergence of net radiative fluxes, and θ_{lobs}, q_{wobs} are derived from observations.

The equation for the cloud droplet number, N_d, is written as

$$\rho\frac{\partial N_\mathrm{d}}{\partial t}=\left[\left(\frac{\lambda_\mathrm{t}}{C_\mathrm{p}}+\frac{\mu_\mathrm{t}}{P_\mathrm{r}}\right)\frac{\partial N_\mathrm{d}}{\partial z}\right]+\rho\left(\frac{\partial N_\mathrm{d}}{\partial t}\right)_{\mathrm{C/E}}+\rho\left(\frac{\partial N_\mathrm{d}}{\partial t}\right)_{\mathrm{NUC}}+\rho\left(\frac{\partial N_\mathrm{d}}{\partial t}\right)_{\mathrm{SED}}, \tag{20}$$

where the subscript SED refers to the rate of change due to sedimentation; C/E to condensation/evaporation; NUC to cloud droplet nucleation respectively. The sink/source terms on the right-hand side are parametrized in terms of the prognostic variables themselves (q_l and N_d).

Determination of the maximum supersaturation $s_{\max}$

$$s_{\max}=\sum_{i=1}^{3}\frac{1}{s_i^2}\left[f_i\left(\frac{\varsigma}{\eta_i}\right)^{3/2}+g_i\left(\frac{s_i^2}{\eta_i+3\varsigma}\right)^{3/4}\right], \tag{21a}$$

with

$$f_i=0.5\exp\left(2.5\ln^2\sigma_i\right), \tag{21b}$$

$$g_i=1+0.25\ln\sigma_i, \tag{21c}$$

$$s_i=\frac{2}{\sqrt{B}}\left(\frac{A}{3r_{\mathrm{a}_i}}\right)^{3/2}, \tag{21d}$$

and

$$\varsigma=\frac{2A}{3}\left(\frac{A_1W+A_3\partial F_\mathrm{rad}/\partial z}{A_4}\right)^{1/2}, \tag{22a}$$

$$\eta_i=\frac{[(A_1W+A_3\partial F_\mathrm{rad}/\partial z)/A_4]^{3/2}}{2\pi\rho_\mathrm{w}A_2N_{\mathrm{a}_i}}, \tag{22b}$$

where ρ_w is the water density, $A_1,\ A_2,\ A_3$ are the constants defined in Eq. 6, and $A_4,\ A,\ B$ can be found in Abdul-Razzak et al. (1998).

References

Archambeau F, Méchitoua N, Sakiz M (2004) Code_Saturne: a finite volume code for the computation of turbulent incompressible flows—industrial applications. Int J Finite 1:1–62

Abdul-Razzak H, Ghan S, Rivora-Carpio C (1998) A parametrization of aerosol activation. 1. Single aerosol types. J Geophys Res 103:6123–6131

Abdul-Razzak H, Ghan S (2000) A parametrization of aerosol activation. 2. Multiple aerosol types. J Geophys Res 105:6837–6844

Bergot T, Carrer D, Noilhan J, Bougeault P (2005) Improved site-specific numerical prediction of fog and low clouds: a feasibility study. Weather Forecast 20:627–646

Bergot T, Terradellas E, Cuxart J, Mira A, Müller OLM, Nielsen N (2007) Intercomparison of single-column numerical models for the prediction of radiation fog. J Appl Meteorol Clim 46:504–521

Bergot T, Haeffelin M, Musson-Genon L, Tardif R, Colomb M, Boitel C, Bouhours G, Bourriane T, Carrer D, Challet J, Chazette P, Drobinski P, Dupont E, Dupont J-C, Elias T, Fesquet C, Garrouste O, Gomes L, Guerin A, Lapouge F, Lefranc Y, Legain D, Morange P, Pietras C, Plana-Fattori A, Protat A, Rangognio J, Raut J-C, Remy S, Richard D, Romand B, Zhang X (2008) Paris-Fog: des chercheurs dans le brouillard. La Météorol 62:48–58

Betts AK (1973) Non-precipitating cumulus convection and its parametrization. Q J R Meteorol Soc 99:178–196

Bott A (1991) On the influence of the physic-chemical properties of aerosols on the life cycle of radiation fogs. Boundary-Layer Meteorol 56:1–31

Bott A, Trautmann T (2002) PAFOG—a new efficient forecast model of radiation fog and low-level stratiform clouds. Atmos Res 64:191–203

Bougeault P (1985) The diurnal cycle of the marine stratocumulus layer: a higher-order model study. J Atmos Sci 42:2826–2843

Bouzereau E, Musson-Genon L, Carissimo B (2008) Application of a semi-spectral cloud water parametrization to cooling tower plumes simulations. Atmos Res 90:78–90

Bouzereau E, Musson-Genon L, Carissimo B (2007) On the definition of the cloud water content fluctuations and its effects on the computation of a second-order liquid water correlation. J Atmos Sci 64:665–669

Brown R, Roach WT (1976) The physic of radiation fog: II—anumerical study. Q J R Meteorol Soc 102:335–354

Brown R (1980) A numerical study of radiation fog with an explicit formulation of the microphysics. Q J R Meteorol Soc 106:781–802

Cohard J, Pinty J, Bedos C (1998) Extending Twomeys analytical estimate of nucleated cloud droplet concentrations from CCN spectra. J Atmos Sci 55:3348–3357

Corradini C, Tonna G (1980) The parameterization of the gravitational water flux in fog models. J. Atmos Sci 37:2535–2539

Cressman GP (1959) An operational objective analysis system. Mon Weather Rev 87:367–374

Deardorff J (1978) Efficient prediction of ground surface temperature and moisture, with inclusion of a layer of vegetation. J Geophys Res 83:1889–1903

Duynkerke P, Driedonks K (1987) Turbulent structure of a shear-driven stratus_topped atmospheric boundary layer: a comparison of model results with observations. J Atmos Sci 45:2343–2451

Duynkerke P (1991) Radiation fog: a comparison of model simulation with detailed observations. Mon Weather Rev 119:324–341

Elias T, Haeffelin M, Drobinski P, Gomes L, Rangognio J, Bergot T, Chazette P, Raut C, Colomb M (2009) Particulate contribution in extinction of visible radiation: pollution, haze and fog. Atmos Res 92:443–454

Fuzzi S, Facchini M, Orsi J, Lind J, Wobrock W, Kessel M, Maser R, Jaeschke W, Enderle K, Arends B, Berner A, Solly I, Kruisz C, Reischl G, Pahd S, Kaminski U, Winkler P, Ogren J, Noone K, Halberg A, Fierlinger O, Oberlinninger H, PuxBaum H, Marzorati A, Hansson H, Wiedensohler A, Svenningsson I, Martinsson B, Schell D, Georggi H (1992) The Po Valley fog experiment 1989: an overview. Tellus 44:448–468

Fuzzi S, Laj P, Ricci L, Orsi G, Heintzenberg J, Wendisch M, Yuskiewicz B, Mertes S, Orsini D, Wiedensohler MSA, Stratmann F, Berg O, Swietlicki E, Frank G, Martinsson B, Günther A, Dierssen J, Schell D, Jaeschke W, Berner A, Dusek U, Galambos Z, Kruisz C, Mesfin S, Wobrock W, Arends B, Brink H (1998) Overview of the Po Valley fog experiment 1994 (CHEMDROP). Contrib Atmos Phys 71:3–19

Guedalia D, Bergot T (1994) Numerical forecasting of radiation fog. Part II: a comparison of model simulation with several observed fog events. Mon Weather Rev 122:1231–1246

Gultepe I, Muller M, Boybeyi Z (2006) A new visibility parametrization for warm-fog applications in numerical weather prediction models. J Appl Meteorol Clim 45:1469–1480

Gultepe I, Tardif R, Michaelides SC, Cermak J, Bott A, Bendix J, Mûller MD, Pagowski M, Hansen B, Ellrod G, Jacobs W, Toth G, Cober SG (2007) Fog research: a review of past achievements and perspectives. Pure Appl Geophys 164:1121–1159

Gultepe I, Pearson G, Milbrandt JA, Hausen B, Platnick S, Taylor P, Gordon M, Oakley JP, Cober SG (2009) The fog remote sensing and modelling field project. Bull Am Meteorol Soc. doi:10.1175/2008BAMS2534: 341–359

Haeffelin M, Bergot T, Elias T, Carrer D, Chazette P, Colomb M, Drobinski P, Dupont J-C, Dupont E, Gomes L, Musson-Genon L, Pietras C, Plana-Fattori A, Protat A, Rangonio J, Raut J-C, Remy S, Richard D, Sciare J, Zhang X (2010) ParisFog, shedding new light on fog physical processes. Bull Am Meteorol Soc 91(6):767–783

Joseph J, Wiscombe W, Weinman J (1976) The delta-Eddington approximation for radiative flux transfer. J Atmos Sci 33:2452–2459

Klemm O, Wrzesinsky P (2007) Fog deposition fluxes of water and ions to a mountainous site in Central Europe. Tellus 59:705–714

Kunkel B (1984) Parameterization of droplet terminal velocity and extinction coefficient in fogs model. J Appl Meteorol 23:34–41

Lacis A, Hansen J (1974) A parametrization for the absorption of solar radiation in the earth's atmosphere. J Atmos Sci 31:118–133

Meyer M, Lala G, Jiusto J (1986) Fog-82: a cooperative field study of radiation fog. Bull Am Meteorol Soc 67:825–832

Müller M, Schmutz C, Parlow E (2007) A one-dimensional ensemble fog forecast and assimilation system for fog prediction. Pure Appl Geophys 164:1241–1264

Musson-Genon L (1987) Numerical simulation of a fog event with a one-dimensional boundary layer model. Mon Weather Rev 115:592–607

Musson-Genon L (1995) Comparison of different simple turbulence closures with an one-dimensional boundary layer model. Mon Weather Rev 123:163–180

Musson-Genon L, Dupont E, Wendum D (2007) Reconstruction of the surface-layer vertical structure from measurements of wind, temperature and humidity at two levels. Boundary-Layer Meteorol 124:235–250

Leighton H (1980) Application to the delta-Eddington method to the absorption of solar radiation in the atmosphere. Atmos Ocean 18:43–52

Nakanishi M (2000) Large-eddy simulation of radiation fog. Boundary-Layer Meteorol 94:461–493

Porson A, Price J, Luck A, Clark P (2011) Radiation fog. Part II: large eddy simulations in very stable conditions. Boundary-Layer Meteorol 139:193–224

Price J (2011) Radiation fog. Part I: observations of stability and drop size distributions. Boundary-Layer Meteorol 139:167–191

Pruppacher HR, Klett JD (1997) Microphysics of clouds and precipitation. Kluwer, Dordrecht

Rangognio J (2009) Impact des aérosols sur le cycle de vie du brouillard, de l'observation à la modélisation. Ph.D. Thesis, Université Paul Sabatier, Toulouse III, 258 pp

Rangognio J, Tullet P, Bergot T, Gomes L, Thouron O, Leriche M (2009) Influence of aerosols on the formation and development of radiation fog. Atmo Phys Chem Dis 9:17963–18019

Ritter A, Regalado CM, Aschan G (2008) Fog water collection in a subtropical Elfin Laurel Forest of the Garajonay National Park (Canary Islands): a combined approach using artificial fog catchers and a physically based impaction model. J Hydrometeorol 9:920–935

Roach WT, Brown R, Caughey SJ, Garland JA, Readings CJ (1976) The physic of radiation fog: I—a field study. Q J R Meteorol Soc 102:313–333

Roquelaure S, Bergot T (2008) A local ensemble prediction system for fog and low clouds: construction, Bayesian model averaging calibration, and validation. J Appl Meteorol Clim 47:3072–3088

Sandu I, Tulet P, Brenguier J (2005) Parametrization of the cloud droplet single scattering albedo based on aerosol chemical composition for LES modelling of boundary layer clouds. Geophys Res Lett 32:19814.1–19814.4

Sartelet KN, Hayami H, Albriet B, Sportisse B (2005) Development and preliminary validation of a Modal Aerosol Model for tropospheric chemistry: MAM. Aerosol Sci Technol 40(2):118–127

Skamarock WC, Klemp JB, Dudhia J, Gill DO, Barker DM, Duda HG, Huang XY, Wang W, Powers JG (2008) A description of the advanced research WRF version 3. NCAR Technical Note, NCAR/TN-475+STR, 113 pp

Seigneur C, Hudischewskyj AB, Seinfeld JH, Whitby KT, Whitby ER, Brock JR, Barnes HM (1986) Simulation of aerosol dynamics: a comparative review of mathematical models. Aerosol Sci Technol 5:205–222

Tardif R (2007) The impact of vertical resolution in the explicit numerical forecasting of radiation fog: a case study. Pure Appl Geophys 164:1221–1240

Tombette M, Chazette P, Sportisse B, Roustan Y (2008) Simulation of aerosol optical properties over Europe with a 3-D size-resolved aerosol model: comparisons with AERONET data. Atmos Chem Phys 8:7115–7132

von Glasow R, Bott A (1999) Interaction of radiation fog with tall vegetation. Atmos Environ 33:1333–1346

Zaïdi H, Dupont E, Milliez M, Musson Genon L, Carissimo B (2012) Numerical simulations of the micro-scale heterogeneities of turbulence observed on a complex site. Boundary-Layer Meteorol 147:237–259

Zhang Y, Seigneur C, Seinfeld JH, Jacobson MZ, Binkowski F (1999) Simulation of aerosol dynamics: a comparative review of algorithms used in air quality models. Aerosol Sci Technol 31:487–514

Zhang L, Gong S, Padro J, Barrie L (2001) A size-segregated particle dry deposition scheme for an atmospheric aerosol module. Atmos Environ 35:549–560